This article has been accepted for inclusion in a future issue of this journal. Content is final as presented, with the exception of pagination.

2021 IEEE International Conference on Robotics and Automation (ICRA 2021)
May 31 - June 4, 2021, Xi'an, China
IEEE TRANSACTIONS ON ROBOTICS   1

Surface-Based Path Following Control: Application of Curved Tapes on 3-D Objects

Christian Hartl-Nesic ⬤, *Member, IEEE*, Tobias Glück ⬤, *Member, IEEE*, and Andreas Kugi ⬤, *Senior Member, IEEE*

Abstract—In this article, a novel approach for the versatile wrinkle-free application of (curved) precut adhesive tapes on freeform 3-D surfaces is presented. Straight and curved tape application paths are mapped onto the 3-D object as geodesics and as lines with imposed geodesic curvature, respectively. The proposed surface-based path following control concept extends the classical path following control by a novel parallel contact frame and a parallel projection operator. Using a static state feedback, the robotic system is transformed into a system with linear input-output behavior in the path coordinates. This allows to traverse a path on a 3-D object with a draping roll without turning around the surface normal vector. The latter prevents distortions and wrinkles of the applied tape. Experimental results with a KUKA LBR iiwa 14 R820 demonstrate the feasibility of the proposed approach.

Index Terms—Deformable material, impedance control, path following control, parallel vector field, tape application.

I. INTRODUCTION

ROBOTIC handling of deformable materials like, e.g., textiles, carbon and glass fiber fabrics, foils, and paper, has been a challenging task in the industry for a long time [1], [2], and has received great attention in research recently [3]. Flexible automation on a human level has not yet been fully achieved for many handling tasks like, e.g., grasping, destacking, and draping. In this context, many specialized mechatronic gripper solutions were implemented for grasping and transporting, see, e.g., [4]–[6]. However, high-mix and low-volume tasks require more flexible solutions.

In the automated tape laying (ATL) and automated fibre placement (AFP), a highly specialized application and consolidation tool is used to mechanically place technical textiles on 3-D surfaces [3]. Due to the tool size and weight, high-payload robots are required for the tool movement and the solution is suitable for large and mostly convex surfaces only. These solutions are limited to continuous material only and precut tapes cannot be processed. In a different approach, called automated part placement (APP), two robots are used for grasping and transporting a deformable (pre-cut) strip, while a third robot consolidates the strip with a draping roll [7]. A force-controlled application of strip-like materials is demonstrated in [7] based on a collaborative path following control concept on a three-arm gantry robot. The commercial solution Samba Pro [8] is able to place small fiber patches using two position-controlled robots. While a six-axis industrial robot positions and orients the 3-D object, a SCARA robot with a soft gripper performs the patch placement. In this solution, however, the patch size as well as the wrapping angle are very limited. Additionally, two- and three-armed APP systems have a limited flexibility since the workspaces of the individual robots have to overlap.

This work presents a novel and flexible approach for impedance-controlled wrinkle-free application of (curved) precut adhesive tapes on freeform 3-D surfaces. The proposed solution uses a single robot with the target 3-D object mounted on the end-effector and a stationary tape-application tool. Thus, the approach provides high flexibility with respect to the shape of the target 3-D objects and the pre-cut tapes, as well as the lay-up location.

From the viewpoint of industrial robotics and classical automation, many processes require the movement of a robot-mounted tool along a given path, whereas the *a priori* time parametrization is an additional degree of freedom [9]. This task is often called *path following control* or contouring control [10], [11] and emerges in processes like, e.g., milling and cutting. In path following control, the current position along the path is determined using a projection operator and transversal feedback linearization allows to linearize the (nonlinear) system with respect to the (nonlinear) path [12], [13]. The resulting system exhibits a linear input-output relation in the path coordinates. Previous works use the FRENET–SERRET frame [14], [15] or the parallel transport frame [16]–[19] for the coordinate transformation. Both frames are not suitable to traverse surfaces, since they are derived from the path directly and do not respect the normal vector field of an underlying surface. On the contrary, surface following control shown in [20] provides a distinct surface normal vector, but the local coordinate frame is derived from the surface only and does not take into account the path tangent vector.

For the application of curved tapes on 3-D objects, a draping tool has to traverse a path on the freeform 3-D surface and
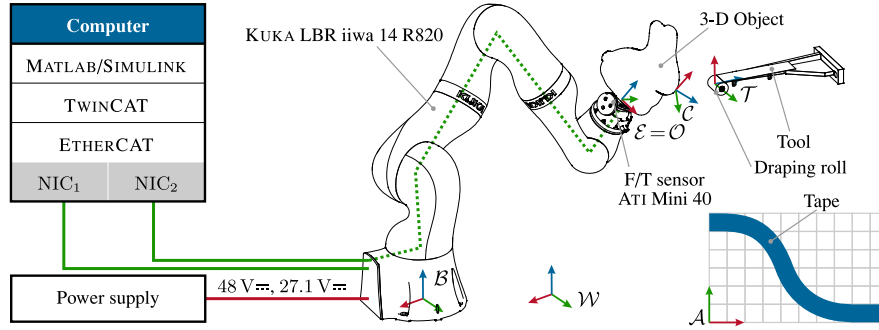
Fig. 1. Schematic drawing of the demonstrator setup and the corresponding (right-handed) coordinate frames.

clearly both the surface normal vector and the path tangent vector are required for a feasible control strategy. To this end, a surface-based path following control concept is developed in this work, which provides a local coordinate frame based on the surface normal and the path tangent. Additionally, the proposed *parallel contact frame* allows to traverse curved paths without turning the draping roll around the surface normal vector to prevent wrinkles in the applied tape. A video demonstrating the results is provided at `www.acin.tuwien.ac.at/52f5`. Furthermore, the algorithms and solutions emerging from this application also represent a solution for a more general robotic problem, i.e. traversing a tool along a curved path on a freeform 3-D surface with defined kinematic constraints. The proposed solution can be used for different applications in the production of textiles, apparel, and consumer goods, in the industry of fiber reinforced plastics for the lay-up of technical textiles, and in the packaging industry.

II. TAPE APPLICATION ON 3-D OBJECTS

This section introduces the demonstrator setup and gives an overview of the tape application process. Moreover, the mathematical model of the robot used in this work is shortly summarized.

A. Experimental Setup

The demonstrator setup, depicted schematically in Fig. 1, consists of the robot KUKA LBR iiwa 14 R820, equipped with the six-axis force/torque (F/T) sensor ATI Mini 40, a desktop computer and a passive, wall-mounted tape application tool with a compliant draping roll. Additionally, a 3-D object is mounted on the tool side of the F/T sensor. The robot and the F/T sensor are interfaced via two network interface cards using the ETHERCAT protocol. The controller is implemented as MATLAB/SIMULINK model, which is executed via the real-time automation software BECKHOFF TWINCAT. The sampling time of the controller, the robot sensors and actuators is $T_{\mathrm{s}} = 125\,\mu\mathrm{s}$, whereas the F/T sensor is sampled with $T_{\mathrm{s,F/T}} = 333\,\mu\mathrm{s}$.

In the following, a few characteristics of the demonstrator setup are given.

1) In contrast to most works in the literature [3], the tool in this work is stationary and the 3-D object is moving. While the relative motion between the tool and the

workpiece is kinematically equivalent, it allows to remove the complex and heavy tape application tool [3] from the robot. Additionally, the tape supply as well as a contouring and separation mechanism can be incorporated into the stationary tool.

2) The F/T sensor is mounted on the robot flange, which is industry standard, and hence, easy to integrate into a robot system.

3) As the 3-D object is mounted on the robot end-effector, the maximum size of the 3-D object is given by the workspace and the maximum payload of the robot.

4) The nonactuated, compliant draping roll allows only to impose normal forces throughout the tape application process. While this is sufficient for many applications [21], [22], adding an additional actuated clamping roll also allows for tape tension forces during the process.

B. Process Overview

Using the previously described demonstrator setup, the tape application process is illustrated in Fig. 2 and consists of the following steps.

1) *2-D tape application path*: A planar tape application path is created on the shape of the planar tape (red line).

2) *3-D path mapping*: The geometry and curvature of the planar tape application path is mapped onto the CAD model of the 3-D object, which creates a 3-D tape application path. Thus, the planar and the 3-D tape application path represent a matching pair of target lines [23].

3) *Robot starting pose*: In order to perform a single continuous draping motion on the 3-D object, a suitable robot starting pose needs to be determined for each tape to be applied. In this work, the complete tape application path is taken into account in this search by simulating the tape application process for a discrete set of feasible initial robot poses. Afterwards, each solution is evaluated with regard to joint velocities (smoothness of the motion), reserves to the joint limits, and collisions. The optimal solution is then used for the experiment. The determination of the robot starting pose is not considered in detail in this work.

4) *Preparation and execution*: The pre-cut tape is placed in the required starting position on the feed of the application
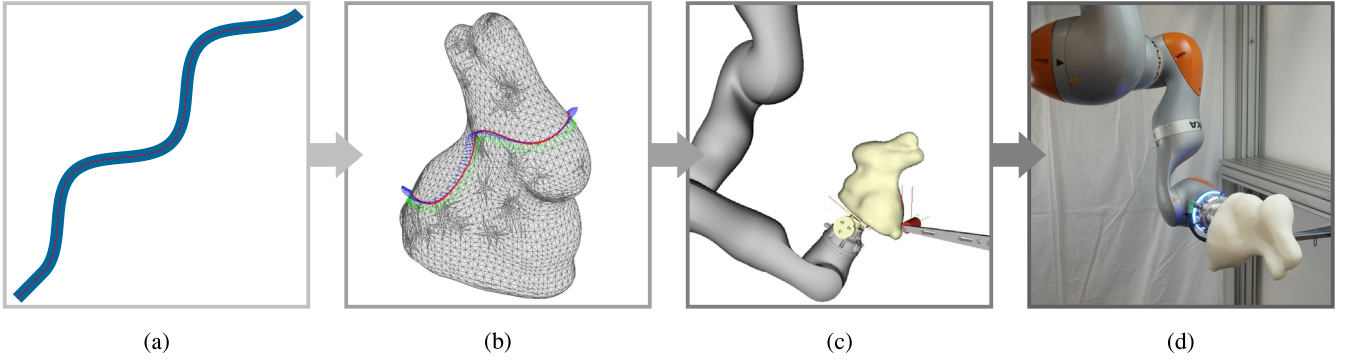
Fig. 2. Tape application process overview. (a) Two-dimensional (2-D) tape application path. (b) Three-dimensional (3-D) path mapping. (c) Robot starting pose. (d) Preparation and execution.

tool and the robot performs the impedance-controlled tape application process.

C. Mathematical Model

The demonstrator setup is described mathematically via the kinematic relations between the coordinate frames, and the dynamic robot model of the KUKA LBR iiwa 14 R820.

1) Coordinate Frames: The (right-handed) coordinate frames in Fig. 1 are denoted by calligraphic letters. The robot base frame $\mathcal{B}$ and the tool frame $\mathcal{T}$ reside stationary in the inertial (world) reference frame $\mathcal{W}$. The y-axis of $\mathcal{T}$ is aligned with the draping roll axis. The target 3-D object is described in the object frame $\mathcal{O}$. This frame coincides with the robot end-effector frame $\mathcal{E}$, which is attached to the tool side of the F/T sensor. The contact frame $\mathcal{C}$ describes the position and orientation of the contact point of the draping roll along the path. The tape in the planar state is described in a separate coordinate system $\mathcal{A}$.

2) Robot Model: The KUKA LBR iiwa 14 R820 is a kinematically redundant light-weight robot, which is modeled with elastic joints with constant stiffness. As shown in [24], the singular perturbation approach is used in conjunction with a static state feedback of the joint torques to obtain

$$\mathbf{M}(\mathbf{q})\ddot{\mathbf{q}} + \mathbf{n}(\mathbf{q}, \dot{\mathbf{q}}) = \boldsymbol{\tau}_{\mathrm{m}} + \boldsymbol{\tau}_{\mathrm{e}} \qquad (1)$$

as the state model. Thus, the result is a standard rigid-body model [25] for the robot link dynamics with the generalized joint coordinates $\mathbf{q}$. Note that $\mathbf{M}(\mathbf{q})$ in (1) is a modified mass matrix, which includes the motor rotor inertias as well as the gain matrices of the static state feedback, see [24]. The nonlinear function $\mathbf{n}(\mathbf{q}, \dot{\mathbf{q}})$ describes the Coriolis and gravitational forces and $\boldsymbol{\tau}_{\mathrm{m}}$ and $\boldsymbol{\tau}_{\mathrm{e}}$ denote the motor torque inputs and the external generalized torques, respectively.

III. PATHS ON SURFACES

Tape application paths on the 3-D object are described as paths on surfaces complemented with the surface normal vector field. For the draping process, the robot motion must prevent turning of the draping roll around the surface normal vector to avoid wrinkles and distortions of the applied tape. The basic terms to

describe the geometric objects in a differential geometric setting are summarized in this section and the concepts of geodesics and curved paths are introduced. Moreover, a novel *parallel contact frame* is derived to account for the requirements of the tape application process.

A. Surfaces

In this work, a surface σ is described in the object frame $\mathcal{O}$ and given by a regular $\mathcal{C}^2$ parametrization $\boldsymbol{\sigma}(\mathbf{s}) : U \subseteq \mathbb{R}^2 \mapsto \mathbb{R}^3$ with the parameter vector $\mathbf{s}^{\mathrm{T}} = [s_1 \quad s_2]$ from an open subset $U \subseteq \mathbb{R}^2$. The parametrization $\boldsymbol{\sigma}(\mathbf{s})$ of a surface σ is called regular if $(\boldsymbol{\sigma}_{s_1} \times \boldsymbol{\sigma}_{s_2})(\bar{\mathbf{s}}) \neq \mathbf{0} \ \forall \bar{\mathbf{s}} \in U$, where $\boldsymbol{\sigma}_{s_i} = \partial \boldsymbol{\sigma}/\partial s_i$ with $i = 1, 2$ are the surface tangential basis vectors [26]. On each regular surface parametrization $\boldsymbol{\sigma}(\mathbf{s})$, a unique unit normal vector field is defined as

$$\boldsymbol{\sigma}_{\mathrm{n}}(\mathbf{s}) = \frac{\boldsymbol{\sigma}_{s_1}(\mathbf{s}) \times \boldsymbol{\sigma}_{s_2}(\mathbf{s})}{\|\boldsymbol{\sigma}_{s_1}(\mathbf{s}) \times \boldsymbol{\sigma}_{s_2}(\mathbf{s})\|_2} , \qquad (2)$$

i.e. the so-called GAUSS map [26].

B. Paths

A path π is given as a parametrized regular $\mathcal{C}^3$ curve $\boldsymbol{\pi}(p) : I \subseteq \mathbb{R} \mapsto \mathbb{R}^3$, described in the object frame $\mathcal{O}$, with the path parameter p from the interval $I \subseteq \mathbb{R}$. For a regular parametrization, $\boldsymbol{\pi}'(\bar{p}) \neq \mathbf{0} \ \forall \bar{p} \in I$ holds [26], where the derivative w.r.t. the path parameter p is denoted as $(\cdot)' = \frac{\partial}{\partial p}(\cdot)$. Additionally, arc-length parametrization is assumed on all paths, i.e. $\|\boldsymbol{\pi}'(p)\|_2 = 1 \ \forall p \in I$.

C. Paths and Vector Fields on Surfaces

A surface-based path π is a path on a surface σ that is assumed to be regularly parametrized by $\boldsymbol{\pi}(p) = \boldsymbol{\sigma}(\mathbf{s}(p))$, with $\mathbf{s}'(p) \neq \mathbf{0}$ $\forall p \in I$.

For clarity of presentation, the arguments of some functions are omitted in the following. The covariant derivative of a vector field along a surface-based path $\boldsymbol{\pi}(p)$ describes the rate of change of this vector field $\mathbf{v}(p)$ projected onto the tangential plane of the surface. If the vector field $\mathbf{v}(p)$ is a surface tangent vector field, i.e. it is a linear combination of the local surface tangential

10123

basis vectors in the form

$$\mathbf{v}(p) = v_1(p)\boldsymbol{\sigma}_{s_1}(\mathbf{s}(p)) + v_2(p)\boldsymbol{\sigma}_{s_2}(\mathbf{s}(p)) , \qquad (3)$$

then the covariant derivative can be expressed in terms of the surface as [26]

$$\frac{\mathrm{D}}{\mathrm{d}p}\mathbf{v} = \left[v_1' + v_1(s_1'\Gamma_{11}^1 + s_2'\Gamma_{12}^1) + v_2(s_1'\Gamma_{21}^1 + s_2'\Gamma_{22}^1) \right] \boldsymbol{\sigma}_{s_1}$$
$$+ \left[v_2' + v_1(s_1'\Gamma_{11}^2 + s_2'\Gamma_{12}^2) + v_2(s_1'\Gamma_{21}^2 + s_2'\Gamma_{22}^2) \right] \boldsymbol{\sigma}_{s_2} , \qquad (4)$$

with $\Gamma_{jk}^i = \Gamma_{kj}^i = \Gamma_{jk}^i(\mathbf{s}(p))$, $i, j, k = 1, 2$ as the CHRISTOFFEL symbols of the surface σ in the parametrization $\boldsymbol{\sigma}(\mathbf{s})$. A vector field $\mathbf{v}(p)$ is called *parallel* [26], if

$$\frac{\mathrm{D}}{\mathrm{d}p}\mathbf{v} = \mathbf{0} \ \ \forall p \in I . \qquad (5)$$

The aforementioned intermediate results are used throughout this work to calculate the necessary geometric objects that describe the motion of a draping roll along a (curved) path on a freeform 3-D surface.

D. Straight Paths: Geodesics

Geodesics are straight paths on surfaces that exhibit no turns around the surface normal vector $\boldsymbol{\sigma}_{\mathrm{n}}$. Therefore, a geodesic describes the desired motion of the draping roll in contact with the surface [27]. A surface-based path $\boldsymbol{\pi}(p)$ is called a geodesic if the path tangent field $\boldsymbol{\pi}'(p)$ is a parallel vector field as defined in (5). With a given starting point $\mathbf{s}_0$ in surface coordinates and a tangent direction $\mathbf{t}_0$, a geodesic can be uniquely calculated according to the following theorem.

Theorem 1 [26]: Given a starting point $\mathbf{s}_0^{\mathrm{T}} = [s_{1,0} \ \ s_{2,0}]$ on the surface σ with the regular parametrization $\boldsymbol{\sigma}(\mathbf{s})$ and a tangent direction $\mathbf{t}_0 = s_{1,0}'\boldsymbol{\sigma}_{s_1} + s_{2,0}'\boldsymbol{\sigma}_{s_2}$, the *unique* geodesic $\boldsymbol{\pi}(p)$, with $\boldsymbol{\pi}(p_0) = \boldsymbol{\sigma}(\mathbf{s}_0)$ and $\boldsymbol{\pi}'(p_0) = \mathbf{t}_0$, is the solution of the initial value problem

$$s_1'' = -s_1'^2\Gamma_{11}^1 - 2\Gamma_{12}^1 s_1' s_2' - s_2'^2\Gamma_{22}^1 \qquad (6a)$$

$$s_2'' = -s_1'^2\Gamma_{11}^2 - 2\Gamma_{12}^2 s_1' s_2' - s_2'^2\Gamma_{22}^2 , \qquad (6b)$$

with the initial conditions

$$s_1(p_0) = s_{1,0} \qquad \qquad s_1'(p_0) = s_{1,0}' \qquad (7a)$$

$$s_2(p_0) = s_{2,0} \qquad \qquad s_2'(p_0) = s_{2,0}' . \qquad (7b)$$

The validity of this theorem can be easily seen by applying the covariant derivative (4) to the tangent vector field of the path $\boldsymbol{\pi}' = \mathbf{v} = s_1'\boldsymbol{\sigma}_{s_1} + s_2'\boldsymbol{\sigma}_{s_2}$. The linear independence of $\boldsymbol{\sigma}_{s_1}$ and $\boldsymbol{\sigma}_{s_2}$ due to the regularity of $\boldsymbol{\sigma}(\mathbf{s})$ yields (6) and the uniqueness can be proven by the PICARD–LINDELÖF theorem, see [28] for more details.

An intuitive choice to construct a contact frame for the tool motion are the (unit) tangent vector $\boldsymbol{\pi}'(p)$, the surface normal vector $\boldsymbol{\sigma}_{\mathrm{n}}(\mathbf{s}(p))$ and their cross product [27]. This contact frame is suitable for applications where the tool orientation has to follow the path tangent, e.g., cutting or sewing, and can also be used for surface-based path following control in Section IV. However, in the tape application process of curved tapes, this
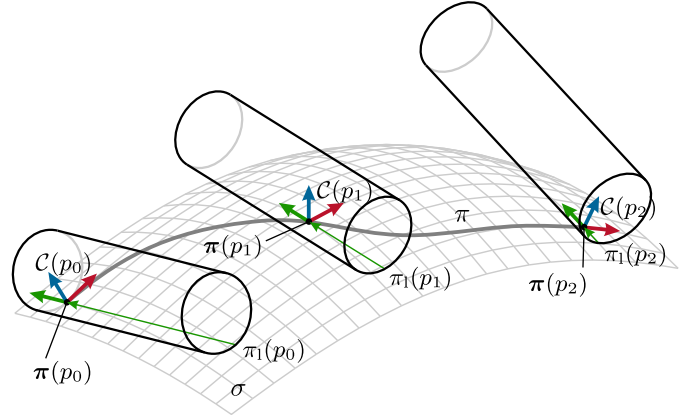

Fig. 3. Evolution of the contact frame $\mathcal{C}$ for a draping process along a curved path π on a doubly-curved surface σ.
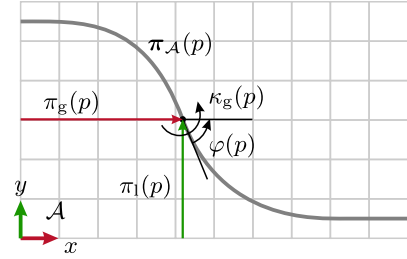

Fig. 4. Geometric relations of the planar path $\boldsymbol{\pi}_{\mathcal{A}}(p)$ in the planar tape coordinate frame $\mathcal{A}$.

choice for the contact frame causes wrinkles and distortions in the applied material, as the path tangent vector $\boldsymbol{\pi}'(p)$ exhibits turns around the surface normal vector. To this end, a new frame is introduced in the next section, which solves these limitations for tape application.

E. Curved Paths

In this section, the aforementioned relations are extended to curved paths. The geometric relationships of a draping motion along a curved path π on a doubly-curved surface σ are illustrated in Fig. 3 for multiple path positions $p_0 < p_1 < p_2$. Instead of rotating the draping roll around the normal vector (blue), which may cause wrinkles and distortions of the tape, the roll is tilted around a particular surface tangent vector (red). The corresponding surface tangent vector field is derived as a *parallel* vector field of the parametrized surface $\boldsymbol{\sigma}(\mathbf{s})$, starting from an initial contact frame $\mathcal{C}(p_0)$. From this parallel vector field and the surface normal vector field, a novel *parallel contact frame* is constructed. This contact frame allows to perform the tape application process for curved paths and prevents wrinkles and lateral tensions in the tape. Moreover, the simple contact frame mentioned in Section III-D emerges as a special case of the parallel contact frame for straight paths.

First, the path geometry is extracted from the planar tape application path $\boldsymbol{\pi}_{\mathcal{A}}(p)$ in the coordinate frame $\mathcal{A}$ according to Fig. 4. Specifically, the geodesic curvature $\kappa_{\mathrm{g}}(p)$ and the lateral

10124

and geodesic position $\pi_l(p)$ and $\pi_g(p)$ of the contact point along the path are calculated. Second, the concept of geodesics on surfaces according to Section III-D is generalized to impose the geodesic curvature $\kappa_g(p)$ locally on the path for every $p \in I$, i.e. the surface-based curve is steered using $\kappa_g(p)$. This results in a parametrized path $\pi(p)$ in the surface coordinates $\mathbf{s}$ of the parametrized surface $\boldsymbol{\sigma}(\mathbf{s})$, i.e. $\pi(p) = \boldsymbol{\sigma}(\mathbf{s}(p))$. Finally, the parallel contact frame $\mathcal{C}(p)$ is constructed as a moving frame along the path $\pi(p)$ based on a parallel vector field. This frame describes the contact point of the draping roll on the surface. Additionally, the resulting frame is well-defined even when the second derivative of the path π'' vanishes.

1) Geodesic Curvature, Lateral and Geodesic Position: The geometric relations in the planar tape coordinate frame $\mathcal{A}$ are depicted in Fig. 4. The arc-length parametrized planar path $\pi_{\mathcal{A}}(p)$, described in $\mathcal{A}$, only exhibits a geodesic curvature $\kappa_g(p)$, which is calculated as [14]

$$\kappa_g(p) = [0 \ \ 0 \ \ 1](\pi'_{\mathcal{A}} \times \pi''_{\mathcal{A}}) . \tag{8}$$

The lateral position $\pi_l(p)$ and the geodesic position $\pi_g(p)$ describe the position of the contact point in the tape coordinate system $\mathcal{A}$. Using the angle between the path tangent and the x-axis in Fig. 4, given by [26]

$$\varphi(p) = \arccos\left([1 \ \ 0 \ \ 0]\pi'_{\mathcal{A}}\right) = \int_0^p \kappa_g(\bar{p}) \, \mathrm{d}\bar{p} , \tag{9}$$

the lateral and geodesic positions are given by

$$\pi_l(p) = \int_0^p \sin(\varphi(\bar{p})) \, \mathrm{d}\bar{p} \tag{10}$$

$$\pi_g(p) = \int_0^p \cos(\varphi(\bar{p})) \, \mathrm{d}\bar{p} . \tag{11}$$

The function $\pi_l(p)$ describes the position of the contact point relative to the draping roll. The geometric relations remain valid, when the underlying path is mapped with the same curvature $\kappa_g(p)$ on a freeform 3-D surface.

Remark 1: The admissible range for the lateral position $\pi_l(p)$ is given by the initial lateral position $\pi_l(p_0)$ and the axial length of the draping roll. Beyond this range, a tape application path is split into multiple parts and the draping roll is repositioned on the surface for each individual part.

Remark 2: The geometry of the draping roll and its compliant surface determine the maximum valley depth for laterally concave areas on the 3-D object.

Remark 3: Section III-E1 also poses a solution to the inverse problem formulation: Given an arc-length parametrized path $\pi(p)$ on a 3-D object, what is the shape of the corresponding planar tape $\pi_{\mathcal{A}}(p)$? To this end, the geodesic curvature $\kappa_g(p)$ of the surface-based path $\pi(p)$ is given by

$$\kappa_g(p) = \boldsymbol{\sigma}_n(\mathbf{s}(p)) \cdot (\pi'(p) \times \pi''(p)) ,$$

and the shape of the arc-length parametrized planar path $\pi_{\mathcal{A}}(p)$ can be computed using (9)–(11).

2) Curved Paths on Surfaces: The geodesic curvature $\kappa_g(p)$ is imposed on the surface-based path $\pi(p)$ in the object frame $\mathcal{O}$ by generalizing the covariant derivative of the path tangent π' according to [26]

$$\left(\frac{\mathrm{D}}{\mathrm{d}p}\pi'\right)(p) = \kappa_g(p)\Big(\boldsymbol{\sigma}_n(\mathbf{s}(p)) \times \pi'(p)\Big), \tag{12}$$

of which the right-hand side is expressed in terms of surface variables as

$$\kappa_g(p)\big(\boldsymbol{\sigma}_n(\mathbf{s}(p)) \times \pi'(p)\big)$$
$$= \kappa_g(p) \left(\frac{\boldsymbol{\sigma}_{s_1} \times \boldsymbol{\sigma}_{s_2}}{\|\boldsymbol{\sigma}_{s_1} \times \boldsymbol{\sigma}_{s_2}\|_2} \times (s'_1\boldsymbol{\sigma}_{s_1} + s'_2\boldsymbol{\sigma}_{s_2}) \right)$$
$$= \kappa_{s_1}(p)\boldsymbol{\sigma}_{s_1} + \kappa_{s_2}(p)\boldsymbol{\sigma}_{s_2}$$

with

$$\kappa_{s_1}(p) = \frac{-\kappa_g(p)}{\|\boldsymbol{\sigma}_{s_1} \times \boldsymbol{\sigma}_{s_2}\|_2}(s'_1\boldsymbol{\sigma}_{s_1} \cdot \boldsymbol{\sigma}_{s_2} + s'_2\boldsymbol{\sigma}_{s_2} \cdot \boldsymbol{\sigma}_{s_2}) \tag{13a}$$

$$\kappa_{s_2}(p) = \frac{\kappa_g(p)}{\|\boldsymbol{\sigma}_{s_1} \times \boldsymbol{\sigma}_{s_2}\|_2}(s'_1\boldsymbol{\sigma}_{s_1} \cdot \boldsymbol{\sigma}_{s_1} + s'_2\boldsymbol{\sigma}_{s_2} \cdot \boldsymbol{\sigma}_{s_1}) . \tag{13b}$$

Following the steps of Theorem 1, a new system of ordinary differential equations can be derived

$$s''_1 = -s'^2_1\Gamma^1_{11} - 2\Gamma^1_{12}s'_1s'_2 - s'^2_2\Gamma^1_{22} + \kappa_{s_1}(p) \tag{14a}$$

$$s''_2 = -s'^2_1\Gamma^2_{11} - 2\Gamma^2_{12}s'_1s'_2 - s'^2_2\Gamma^2_{22} + \kappa_{s_2}(p) , \tag{14b}$$

with the initial values (7), which allows to steer the path locally using the path curvature $\kappa_g(p)$ via $\kappa_{s_1}(p)$ and $\kappa_{s_2}(p)$. The solution of (14) is the planar curve $\pi_{\mathcal{A}}(p)$ from the planar tape coordinate frame $\mathcal{A}$ mapped onto the surface σ in the surface coordinates $\mathbf{s}(p)$ with a given starting point $\mathbf{s}_0$ and tangent direction $\mathbf{t}_0$.

3) Parallel Contact Frame: The parallel contact frame is constructed using the surface normal vector field $\pi_n(p) = \boldsymbol{\sigma}_n(\mathbf{s}(p))$ and a parallel vector field $\pi_t(p)$. Thus, using (4) and (5) with $\mathbf{v} = \pi_t(p) = t_1\boldsymbol{\sigma}_{s_1} + t_2\boldsymbol{\sigma}_{s_2}$ leads to the first-order differential equations

$$t'_1 = -t_1(s'_1\Gamma^1_{11} + s'_2\Gamma^1_{12}) - t_2(s'_1\Gamma^1_{21} + s'_2\Gamma^1_{22}) \tag{15a}$$

$$t'_2 = -t_1(s'_1\Gamma^2_{11} + s'_2\Gamma^2_{12}) - t_2(s'_1\Gamma^2_{21} + s'_2\Gamma^2_{22}) , \tag{15b}$$

from which the parallel unit vector field $\pi_t(p)$ is calculated. The initial conditions $t_1(p_0)$ and $t_2(p_0)$ are chosen such that $\pi_t(p_0) = \pi'(p_0)$. The third unit vector field $\pi_b = \pi_t \times \boldsymbol{\sigma}_n$ completes the parallel contact frame $(\pi_t, \pi_b, \pi_n)(p)$, which is also denoted as $\mathcal{C}(p)$. The resulting frame precisely describes the motion of the draping roll along the path, i.e. it prevents rotations around the surface normal vector field $\boldsymbol{\sigma}_n(p)$ while performing tilting motions around the parallel unit vector field $\pi_t(p)$ to traverse the contact point in lateral direction.

Remark 4: In contrast, the draping roll paths in [29] originate from a surface-plane intersection strategy that yields non-geodesic paths. Thus, the contact frame exhibits turns around the surface normal vector. This introduces strain into the applied material, which should be prevented for the considered application. Similarly, [27] incorporates friction forces when winding fibre strands to allow for so-called quasi-geodesic paths.
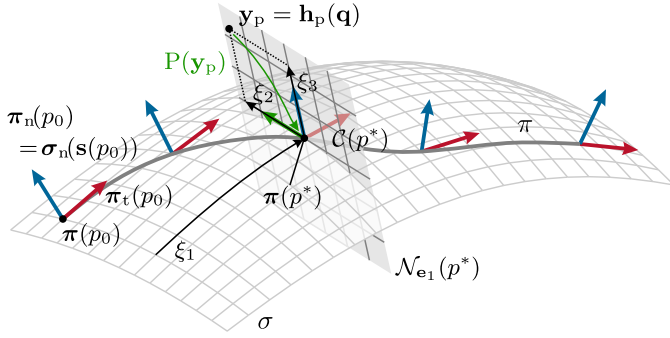
10125

Fig. 5.   Geometric objects of surface based path following control.

IV. Surface-Based Path Following Control

In path following control, the robot motion is described by a path π, which determines the geometry in space, and the path parameter p, which specifies the position along the path. In this section, surface-based path following control is proposed, which extends the classical concepts of path following control, see [15] and [17], to paths with a given surface normal vector field.

The basic components and geometric objects of surface-based path following control are summarized in Fig. 5. The path parametrization $\boldsymbol{\pi}(p) = \boldsymbol{\sigma}(\mathbf{s}(p))$ is complemented with the surface normal vector field $\boldsymbol{\pi}_{\mathrm{n}}(p) = \boldsymbol{\sigma}_{\mathrm{n}}(\mathbf{s}(p))$, a parallel tangent vector field $\boldsymbol{\pi}_{\mathrm{t}}(p)$ and a binormal vector field $\boldsymbol{\pi}_{\mathrm{b}}(p)$ according to Section III-E3. The parallel contact frame $\mathcal{C}(p)$ is constructed at each point p along the path using

$$(\mathbf{e}_1, \mathbf{e}_2, \mathbf{e}_3)\,(p) = (\boldsymbol{\pi}_{\mathrm{t}}, \boldsymbol{\pi}_{\mathrm{b}}, \boldsymbol{\pi}_{\mathrm{n}})\,(p). \tag{16}$$

The current path position p^* is determined by a projection operator $\mathrm{P}(\mathbf{y}_{\mathrm{p}})$, which is defined later in this section, from the output position $\mathbf{y}_{\mathrm{p}}$ of the robotic system. Based on the projected contact frame $\mathcal{C}(p^*)$, a coordinate transformation and a static state feedback is derived. The resulting system exhibits a linear input-output behavior in path coordinates and serves as a basis for the design of the task space and nullspace controllers.

In previous works, e.g., [17] and [20], the coordinate transformation results from a parallel transport frame, which evolves from a system of differential-algebraic equations along the path. Thus, the surface normal vector can only be specified at the initial position on the path, whereas surface-based path following control presented in this article allows to fix the surface normal vector at each position along the path. Similarly, the Frenet–Serret frame used in [15] derives from the path geometry directly and does not allow to specify a surface normal vector.

A. Output Function

As shown in Fig. 1, the demonstrator setup uses a fixed tool frame $\mathcal{T}$, whereas the path is attached to the 3-D object in the object frame $\mathcal{O}$, which moves with the end-effector frame $\mathcal{E}$. In terms of homogeneous transformations [25], the kinematic relations are described as

$$\mathbf{H}_{\mathcal{O}}^{\mathcal{T}}(\mathbf{q}) = \mathbf{H}_{\mathcal{O}}^{\mathcal{E}}\mathbf{H}_{\mathcal{E}}^{\mathcal{B}}(\mathbf{q})\mathbf{H}_{\mathcal{B}}^{\mathcal{W}}\mathbf{H}_{\mathcal{W}}^{\mathcal{T}}\,, \tag{17}$$

where $\mathbf{H}_{\mathcal{X}}^{\mathcal{Y}}$ is the homogeneous representation of the coordinate frame $\mathcal{Y}$ with respect to $\mathcal{X}$, expressed in $\mathcal{X}$. In this setup, $\mathcal{E} = \mathcal{O}$ and thus, $\mathbf{H}_{\mathcal{O}}^{\mathcal{E}}$ is equal to the identity matrix. Based on (17), the output $\mathbf{y} \in \mathbb{R}^6$ of the system (1) is chosen as Cartesian position $\mathbf{y}_{\mathrm{p}} \in \mathbb{R}^3$ and orientation $\mathbf{y}_{\mathrm{o}} \in \mathbb{R}^3$ of the tool frame $\mathcal{T}$ with respect to the object frame $\mathcal{O}$

$$\mathbf{y} = \begin{bmatrix} \mathbf{y}_{\mathrm{p}} \\ \mathbf{y}_{\mathrm{o}} \end{bmatrix} = \begin{bmatrix} \mathbf{h}_{\mathrm{p}}(\mathbf{q}) \\ \mathbf{h}_{\mathrm{o}}(\mathbf{q}) \end{bmatrix} = \mathbf{h}(\mathbf{q})\,. \tag{18}$$

Thus, $\mathbf{h}(\mathbf{q})$ is a sufficiently smooth function of the generalized coordinates $\mathbf{q}$. Note that $\mathbf{y}_{\mathrm{o}}$ is a minimal representation for the orientation, e.g., Euler angles, and a suitable convention has to be chosen to avoid representation singularities. The first and second derivative of (18) are computed using the Jacobian

$$\mathbf{J}(\mathbf{q}) = \left(\frac{\partial \mathbf{h}}{\partial \mathbf{q}}\right)(\mathbf{q}) = \begin{bmatrix} \mathbf{J}_{\mathrm{p}}(\mathbf{q}) \\ \mathbf{J}_{\mathrm{o}}(\mathbf{q}) \end{bmatrix} \tag{19}$$

as

$$\dot{\mathbf{y}} = \mathbf{J}(\mathbf{q})\dot{\mathbf{q}} \tag{20}$$

$$\ddot{\mathbf{y}} = \dot{\mathbf{J}}(\mathbf{q}, \dot{\mathbf{q}})\dot{\mathbf{q}} + \mathbf{J}(\mathbf{q})\ddot{\mathbf{q}}\,. \tag{21}$$

B. Parallel Projection Operator

The *parallel* projection operator $\mathrm{P}(\mathbf{y}_{\mathrm{p}})$ used in this work determines the current position p^* on the path while respecting the parallel contact frame given in (16). In this way, the draping roll orientation and the lateral contact point motion $\pi_{\mathrm{l}}(p)$ are taken into account. The operator $\mathrm{P}(\mathbf{y}_{\mathrm{p}})$ projects the output position $\mathbf{y}_{\mathrm{p}}$ onto that point $\boldsymbol{\pi}(p^*)$ on the path where the plane $\mathcal{N}_{\mathbf{e}_1}(p^*) = \{\mathbf{x} \in \mathbb{R}^3 \,|\, \mathbf{x} - \boldsymbol{\pi}(p^*) \perp \mathbf{e}_1(p^*)\}$ intersects the path, i.e. the condition

$$(\mathbf{y}_{\mathrm{p}} - \boldsymbol{\pi}(p^*))^{\mathrm{T}}\mathbf{e}_1(p^*) = 0 \tag{22}$$

is fulfilled, see Fig. 5. In case multiple solutions exist, the one with the smallest distance $\|\mathbf{y}_{\mathrm{p}} - \boldsymbol{\pi}(p^*)\|_2$ is chosen. In contrast, projection operators in previous works project by a minimum-distance criterion only [17]. Taking the time derivative of the constraint (22) and solving for $\dot{p}^*$ leads to

$$\dot{p}^* = \beta(\mathbf{y}_{\mathrm{p}})\mathbf{e}_1^{\mathrm{T}}(p^*)\mathbf{J}_{\mathrm{p}}(\mathbf{q})\dot{\mathbf{q}}\,, \tag{23}$$

with

$$\beta(\mathbf{y}_{\mathrm{p}}) = \frac{1}{\mathbf{e}_1^{\mathrm{T}}(p^*)\boldsymbol{\pi}'(p^*) - (\mathbf{y}_{\mathrm{p}} - \boldsymbol{\pi}(p^*))^{\mathrm{T}}\mathbf{e}_1'(p^*)}\,. \tag{24}$$

C. Coordinate Transformation

Using the parallel contact frame (16) and the parallel projection operator $\mathrm{P}(\mathbf{y}_{\mathrm{p}})$ with (22), the system output $\mathbf{y}$ is uniquely

transformed to new path-based coordinates

$$\hat{\mathbf{y}} = \begin{bmatrix} \boldsymbol{\xi}_{\mathrm{p}} \\ \boldsymbol{\xi}_{\mathrm{o}} \end{bmatrix} = \begin{bmatrix} \xi_1 \\ \vdots \\ \xi_6 \end{bmatrix}, \tag{25}$$

where $\boldsymbol{\xi}_{\mathrm{p}} \in \mathbb{R}^3$ denotes the position w.r.t. the path $\boldsymbol{\pi}(p)$ and $\boldsymbol{\xi}_{\mathrm{o}} \in \mathbb{R}^3$ is the orientation relative to the contact frame $\mathcal{C}(p^*)$. In the following, the new coordinates $\hat{\mathbf{y}}$, organized in the tangential, transversal, and orientation subsystem, are derived.

1) Tangential Subsystem: The tangential coordinate ξ_1 is chosen as the geodesic position $\pi_{\mathrm{g}}(p^*)$ along the path, i.e. in terms of surface geometry this is

$$\xi_1 = \int_{p_0}^{p^*} \left(\boldsymbol{\pi}'(\bar{p})\right)^{\mathrm{T}} \mathbf{e}_1(\bar{p}) \, \mathrm{d}\bar{p}, \tag{26}$$

with the time derivative, see (23)

$$\begin{aligned}\dot{\xi}_1 &= \left(\boldsymbol{\pi}'(p^*)\right)^{\mathrm{T}} \mathbf{e}_1(p^*)\dot{p}^* \\ &= \left(\boldsymbol{\pi}'(p^*)\right)^{\mathrm{T}} \mathbf{e}_1(p^*)\beta(\mathbf{y}_{\mathrm{p}})\mathbf{e}_1^{\mathrm{T}}(p^*)\mathbf{J}_{\mathrm{p}}(\mathbf{q})\dot{\mathbf{q}}. \end{aligned} \tag{27}$$

2) Transversal Subsystem: As shown in Fig. 5, the transversal coordinates ξ_2 and ξ_3 are calculated as projections of the parallel distance vector $\mathbf{y}_{\mathrm{p}} - \boldsymbol{\pi}(p^*)$ onto the coordinate axes $\mathbf{e}_2(p^*)$ and $\mathbf{e}_3(p^*)$, respectively, i.e.

$$\xi_i = \mathbf{e}_i^{\mathrm{T}}(p^*)\left(\mathbf{y}_{\mathrm{p}} - \boldsymbol{\pi}(p^*)\right), \quad i = 2, 3. \tag{28}$$

The corresponding velocities read as

$$\dot{\xi}_i = \left(\alpha_i(\mathbf{y}_{\mathrm{p}})\mathbf{e}_1^{\mathrm{T}}(p^*) + \mathbf{e}_i^{\mathrm{T}}(p^*)\right)\mathbf{J}_{\mathrm{p}}(\mathbf{q})\dot{\mathbf{q}}, \tag{29}$$

with

$$\alpha_i(\mathbf{y}_{\mathrm{p}}) = \beta(\mathbf{y}_{\mathrm{p}})\left(\left(\mathbf{e}_i'(p^*)\right)^{\mathrm{T}}(\mathbf{y}_{\mathrm{p}} - \boldsymbol{\pi}(p^*)) - \mathbf{e}_i^{\mathrm{T}}(p^*)\boldsymbol{\pi}'(p^*)\right)$$

for $i = 2, 3$. Note that the parallel transport frame used in [17] prevents twists of $\mathbf{e}_2(p)$ and $\mathbf{e}_3(p)$ around the path tangent vector, which allows for further simplifications in (29) due to the geometric relations of the frame, i.e. $\alpha_i(\mathbf{y}_{\mathrm{p}}) = 0$. In contrast, the surface-based parallel contact frame (16) allows for twists around the tangent vector, and thus, no further simplifications can be made.

3) Orientation Subsystem: The three coordinates of the orientation $\boldsymbol{\xi}_{\mathrm{o}}$ are chosen as deviation of the output orientation $\mathbf{y}_{\mathrm{o}}$ from the orientation of the parallel contact frame (16), denoted by $\boldsymbol{\pi}_{\mathrm{o}}(p^*)$, as

$$\boldsymbol{\xi}_{\mathrm{o}} = \mathbf{y}_{\mathrm{o}} - \boldsymbol{\pi}_{\mathrm{o}}(p^*) = \mathbf{h}_{\mathrm{o}}(\mathbf{q}) - \boldsymbol{\pi}_{\mathrm{o}}(p^*) \tag{30}$$

and the corresponding time derivative yields

$$\begin{aligned}\dot{\boldsymbol{\xi}}_{\mathrm{o}} &= \dot{\mathbf{y}}_{\mathrm{o}} - \boldsymbol{\pi}_{\mathrm{o}}'(p^*)\dot{p}^* \\ &= \big(\mathbf{J}_{\mathrm{o}}(\mathbf{q}) - \underbrace{\boldsymbol{\pi}_{\mathrm{o}}'(p^*)\beta(\mathbf{y}_{\mathrm{p}})\mathbf{e}_1^{\mathrm{T}}(p^*)}_{\boldsymbol{\Lambda}(\mathbf{y}_{\mathrm{p}})}\mathbf{J}_{\mathrm{p}}(\mathbf{q})\big)\dot{\mathbf{q}}. \end{aligned} \tag{31}$$

4) Coordinate Transformation: The aforementioned relations are assembled into a new virtual output $\hat{\mathbf{y}}$ and its time

derivative $\dot{\hat{\mathbf{y}}}$ using the transformed coordinates

$$\hat{\mathbf{y}} = \begin{bmatrix} \xi_1 \\ \xi_2 \\ \xi_3 \\ \boldsymbol{\xi}_{\mathrm{o}} \end{bmatrix} = \begin{bmatrix} (26) \\ (28)|_{i=2} \\ (28)|_{i=3} \\ (30) \end{bmatrix}$$

$$\dot{\hat{\mathbf{y}}} = \begin{bmatrix} \dot{\xi}_1 \\ \dot{\xi}_2 \\ \dot{\xi}_3 \\ \dot{\boldsymbol{\xi}}_{\mathrm{o}} \end{bmatrix} = \underbrace{\underbrace{\begin{bmatrix} (\boldsymbol{\pi}'(p^*))^{\mathrm{T}} \mathbf{e}_1(p^*)\beta(\mathbf{y}_{\mathrm{p}})\mathbf{e}_1^{\mathrm{T}}(p^*) & \mathbf{0} \\ \alpha_2(\mathbf{y}_{\mathrm{p}})\mathbf{e}_1^{\mathrm{T}}(p^*) + \mathbf{e}_2^{\mathrm{T}}(p^*) & \mathbf{0} \\ \alpha_3(\mathbf{y}_{\mathrm{p}})\mathbf{e}_1^{\mathrm{T}}(p^*) + \mathbf{e}_3^{\mathrm{T}}(p^*) & \mathbf{0} \\ -\boldsymbol{\Lambda}(\mathbf{y}_{\mathrm{p}}) & \mathbf{I} \end{bmatrix}}_{\mathbf{L}(\mathbf{q})} \underbrace{\begin{bmatrix} \mathbf{J}_{\mathrm{p}}(\mathbf{q}) \\ \mathbf{J}_{\mathrm{o}}(\mathbf{q}) \end{bmatrix}}_{\mathbf{J}(\mathbf{q})}}_{\hat{\mathbf{J}}(\mathbf{q})} \dot{\mathbf{q}}. \tag{32}$$

Note that in $\dot{\hat{\mathbf{y}}}$, the geometry of the path and the surface appear in form of an additional transformation matrix $\mathbf{L}(\mathbf{q})$ in $\hat{\mathbf{J}}(\mathbf{q})$, cf. (20).

Remark 5: At points where the tape application path $\boldsymbol{\pi}(p)$ has in-plane turns, the path tangent $\boldsymbol{\pi}'(p)$ lies in the $(\mathbf{e}_2, \mathbf{e}_3)$-plane of the parallel contact frame $\mathcal{C}(p)$ and becomes orthogonal to the geodesic direction $\mathbf{e}_1 \perp \boldsymbol{\pi}'$. Thus, the regularity of $\mathbf{L}(\mathbf{q})$ is lost at turning points. Such paths have to be split into multiple separate segments to exclude turning points.

In the absence of turning points (see Remark 5), the transformation matrix $\mathbf{L}(\mathbf{q})$ is nonsingular, which ensures a unique transformation from the system output $\mathbf{y}$ to the new path-based coordinates $\hat{\mathbf{y}}$. The considered robot KUKA LBR iiwa 14 R820 exhibits seven degrees of freedom, i.e. $\dim(\mathbf{q}) = 7$, and thus, the transformed system has a 6-D task space $\hat{\mathbf{y}}$ and a 1-D nullspace.

D. Feedback Linearization

The state feedback

$$\boldsymbol{\tau}_{\mathrm{m}} = \mathbf{M}(\mathbf{q}) \left(\hat{\mathbf{J}}^{\dagger}(\mathbf{q}) \left(\mathbf{v} - \dot{\hat{\mathbf{J}}}(\mathbf{q}, \dot{\mathbf{q}})\dot{\mathbf{q}} \right) + \mathbf{v}_{\mathrm{n}} \right) + \mathbf{n}(\mathbf{q}, \dot{\mathbf{q}}) - \boldsymbol{\tau}_{\mathrm{e}} \tag{33}$$

with the new system input $\mathbf{v}^{\mathrm{T}} = [\mathbf{v}_{\mathrm{p}}^{\mathrm{T}} \ \mathbf{v}_{\mathrm{o}}^{\mathrm{T}}] = [v_1 \ \cdots \ v_6]$ transforms the system (1) into a system with linear input-output behavior in the new path-based coordinates

$$\ddot{\hat{\mathbf{y}}} = \mathbf{v}. \tag{34}$$

Due to the kinematic redundancy of the robot, the right pseudoinverse of the Jacobian matrix $\hat{\mathbf{J}}^{\dagger}(\mathbf{q}) = \hat{\mathbf{J}}^{\mathrm{T}}(\mathbf{q})(\hat{\mathbf{J}}(\mathbf{q})\hat{\mathbf{J}}^{\mathrm{T}}(\mathbf{q}))^{-1}$ is used in (33). The second system input $\mathbf{v}_{\mathrm{n}}$ of (33) acts on the nullspace of the nonsquare Jacobian matrix $\hat{\mathbf{J}}(\mathbf{q})$ and will be detailed in Section IV-F.

E. Task Space Controller

For the interaction task between the 3-D object and the draping roll, an impedance controller is implemented

$$\mathbf{v} = \ddot{\hat{\mathbf{y}}}^{\mathrm{d}} + \left(\mathbf{M}^{\mathrm{d}}\right)^{-1} \left(\hat{\mathbf{f}}_{\mathrm{e}} - \mathbf{D}^{\mathrm{d}}\dot{\hat{\mathbf{e}}} - \mathbf{K}^{\mathrm{d}}\hat{\mathbf{e}}\right), \tag{35}$$

with the desired diagonal mass matrix $\mathbf{M}^{\mathrm{d}} = \mathrm{diag}(m_1^{\mathrm{d}}, \ldots, m_6^{\mathrm{d}})$, the damping matrix $\mathbf{D}^{\mathrm{d}} = \mathrm{diag}(d_1^{\mathrm{d}}, \ldots, d_6^{\mathrm{d}})$, and the stiffness

matrix $\mathbf{K}^{\mathrm{d}} = \mathrm{diag}(k_1^{\mathrm{d}}, \ldots, k_6^{\mathrm{d}})$. Additionally, the control error $\hat{\mathbf{e}} = \hat{\mathbf{y}} - \hat{\mathbf{y}}^{\mathrm{d}}$ w.r.t. the desired trajectory $(\hat{\mathbf{y}}^{\mathrm{d}})^{\mathrm{T}} = [\xi_1^{\mathrm{d}} \quad \cdots \quad \xi_6^{\mathrm{d}}]$ and the external forces in the contact point $\hat{\mathbf{f}}_{\mathrm{e}}^{\mathrm{T}} = \boldsymbol{\tau}_{\mathrm{e}}^{\mathrm{T}} \hat{\mathbf{J}}^{\dagger}(\mathbf{q})$ are introduced. The linear task space controller (35) acts on the input–output linearized system (34) with the virtual input $\mathbf{v}$. The closed-loop system is stable for $m_i^{\mathrm{d}} > 0$, $k_i^{\mathrm{d}} > 0$, $d_i^{\mathrm{d}} > 0$, $i = 1, 2, \ldots, 6$.

The chosen control scheme is robust against errors in the tangential and lateral position, as well as in the orientation using the impedance controller. The tape application path is traversed with a suitable trajectory for ξ_1^{d}. The desired trajectory ξ_3^{d} specifies the draping roll motion along the surface normal vector and allows to approach the 3-D object, establish and release the contact with the 3-D object. Additionally, the tape application normal force is adjusted using the impedance parameters m_3^{d}, k_3^{d}, and d_3^{d} of the coordinate ξ_3. Finally, the draping roll axis is—in the absence of control errors—aligned to the $\mathbf{e}_2$-axis of the contact frame $\mathcal{C}(p^*)$, see Fig. 3. Thus, choosing $\xi_2^{\mathrm{d}} = -\pi_1(p^*)$ for the lateral motion of the draping roll (see Fig. 4) correctly takes into account the lateral movement of the contact point and prevents a lateral sliding motion of the draping roll. Instead, the roll is tilted parallel to the $\mathbf{e}_2$-axis of the contact frame and the contact point traverses in the lateral direction appropriately.

F. Nullspace Controller

The 1-D nullspace of the redundant robot, i.e. the elbow position, is stabilized using a complementary projection matrix and a simple proportional-derivative controller [24], reading as

$$\mathbf{v}_{\mathrm{n}} = \left(\mathbf{I} - \hat{\mathbf{J}}^{\dagger}(\mathbf{q})\hat{\mathbf{J}}(\mathbf{q})\right) \left(-\mathbf{D}_{\mathrm{n}}\dot{\mathbf{q}} - \mathbf{K}_{\mathrm{n}}(\mathbf{q} - \mathbf{q}_0)\right) , \qquad (36)$$

with the positive definite controller gain matrices $\mathbf{K}_{\mathrm{n}}$ and $\mathbf{D}_{\mathrm{n}}$ and a virtual equilibrium joint position $\mathbf{q}_0$. The stability properties of (hierarchical) projection-based nullspace controllers are given in [30] and the references therein.

For the application at hand, the cylindrical shape of the draping roll provides an additional redundancy in the output space of the robot. During the tape application process, the contact point on the draping roll may move freely on the circumference of the roll. Thus, trajectory planning for a draping motion can exploit this redundancy and steer the contact point to provide more flexibility w.r.t. the shapes of the paths and the 3-D objects.

Alternatively, the aforementioned redundancy in the output space of the robot allows to transfer this degree of freedom from the task space to the nullspace, which increases the nullspace dimension by one. This 2-D nullspace can be controlled by a hierarchical nullspace controller [30]. This way, the contact point between the target 3-D object and the draping roll as well as the robot elbow position can be adjusted automatically by the nullspace controller. The desired robot motion in the nullspace is then specified by suitable nullspace objective functions [25] and the respective controller parameters. Thus, trajectory planning for the tape application process is reduced to finding a feasible robot starting pose as described in Section II-B. Note that the
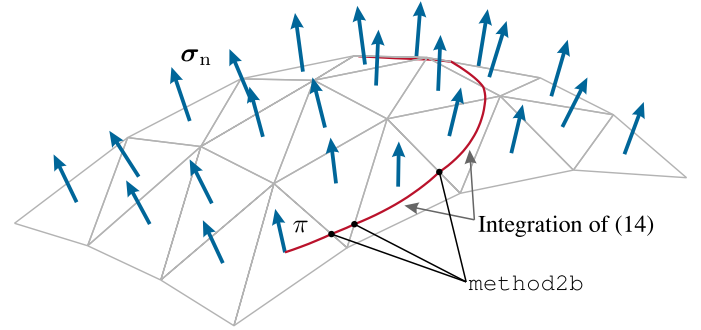

Fig. 6. Triangle mesh surface with surface normal field $\boldsymbol{\sigma}_{\mathrm{n}}$ and path π. The path π is calculated by piecewise integration of (14) and using method2b [31].

details of the nullspace control are beyond the scope of this article.

V. IMPLEMENTATION

In this section, the proposed control approach is applied to the demonstrator setup depicted in Fig. 1. The controllers are implemented as MATLAB/SIMULINK modules, which are executed via the real-time automation software BECKHOFF TWINCAT on a desktop computer.

For the practical implementation, a spatial discretization of the 3-D objects must be performed and the control algorithms have to be implemented in discrete time with the sampling time T_{s}. In the following, the index k of a quantity refers to the time $t = kT_{\mathrm{s}}$, $k = 0, 1, 2, \ldots$, i.e. $\xi_k = \xi(t)|_{t=kT_{\mathrm{s}}}$. In this section, discrete-space paths and surfaces are introduced first and based on this, the discrete-time version of the surface-based path following control is derived.

A. Discrete Paths and Surfaces

A discrete surface consists of a set of triangles, which are interconnected by common edges and vertices. Given a starting point $\boldsymbol{\sigma}(\mathbf{s}_0)$ on the surface and a tangent direction $\mathbf{t}_0$, Algorithm 1 maps the planar path from the tape coordinate frame $\mathcal{A}$ (see Fig. 4) to the 3-D object, as illustrated in Fig. 6. Each triangle has a distinct normal vector $\boldsymbol{\sigma}_{\mathrm{n}}$ and is equipped with local coordinates. By piecewise integration of (14), a continuous tape application path is calculated on each triangle. At the edges and vertices, the adjacent triangle and the corresponding starting point and tangent direction are found using method2b [31]. Note that the accuracy of the computed tape application path significantly depends on the tessellation tolerance, with which the discrete surface is generated [31]. A smaller tessellation tolerance yields more accurate discrete surfaces and tape application paths. The integration of (14) is performed on the triangles of the discrete surface, which are essentially planes. Thus, the relations $\Gamma_{jk}^i = 0 \ \forall i, j, k = 1, 2$ and $\boldsymbol{\sigma}_{s_i} \cdot \boldsymbol{\sigma}_{s_j} = \delta_{ij}$ hold with the KRONECKER delta δ_{ij} and (14) simplifies to two double integrators driven by the terms $\kappa_{s_1}(p)$ and $\kappa_{s_2}(p)$. Hence, high accuracy for the integration of (14) can be achieved using higher order integration algorithms, e.g. the explicit RUNGE–KUTTA

This article has been accepted for inclusion in a future issue of this journal. Content is final as presented, with the exception of pagination.

HARTL-NESIC *et al.*: SURFACE-BASED PATH FOLLOWING CONTROL

9

Algorithm 1: Map Curved Path on Discrete Surface.

1:    Initialize $\boldsymbol{\pi}(p_0) = \boldsymbol{\sigma}(\mathbf{s}_0)$
2:    Initialize $\boldsymbol{\pi}'(p_0) = \mathbf{t}_0$
3:    Find initial triangle containing $\boldsymbol{\pi}(p_0)$
4:    **for all** $p \in I$ **do**
5:       $\mathbf{s}_0 \leftarrow$ Current position $\boldsymbol{\pi}(p)$ in triangle coordinates
6:       $\mathbf{s}_0' \leftarrow$ Current tangent $\boldsymbol{\pi}'(p)$ in triangle coordinates
7:       Integrate (14) using $\kappa_{\mathrm{g}}(p)$ until an edge or vertex is reached at $p = p_{\mathrm{e}}$
8:       $\boldsymbol{\pi}(p_{\mathrm{e}}) \leftarrow \boldsymbol{\sigma}([s_1 \quad s_2]^{\mathrm{T}})$
9:       $\boldsymbol{\pi}'(p_{\mathrm{e}}) \leftarrow s_1'\boldsymbol{\sigma}_{s_1} + s_2'\boldsymbol{\sigma}_{s_2}$
10:      Transition to adjacent triangle using `method2b` [31]
11:   **end for**

(4,5) formula [32]. Additionally, as the discrete surface, and thus, the resulting path are of class $\mathcal{C}^0$ due to the vertices and edges between the triangles, the path has to be further smoothed before applying the control strategy.

B. Discrete Surface-Based Path Following Control

The path is sampled equidistantly with a grid spacing of Δp and the sampled points are interpolated using $\mathcal{C}^3$ B-splines [33] to satisfy the smoothness requirements for the control strategy. To interpolate the corresponding normal vectors, quaternions in the *cumulative form* [34] are used. In this form, quaternions are composed of an initial quaternion and a sequence of angular rotations, which are activated smoothly and sequentially by real-valued basis functions. The resulting path $\boldsymbol{\pi}(p)$ and the normal vector field $\boldsymbol{\pi}_{\mathrm{n}}(p)$ are used to construct the parallel contact frame. In this work, the implementation of the task space and nullspace controllers use quaternions to parametrize the orientation. Thus, the geometric Jacobian matrix is used in (33) and in the subsequent equations [25]. Moreover, discretized implementations for the projection operator $\mathrm{P}(\mathbf{y}_{\mathrm{p}})$ with the condition (22), the parallel contact frame (16) and the integral (26) are developed in the following to be solved in real time.

1) Surface-Based Orthonormalized Frame: As the path $\boldsymbol{\pi}(p)$ and its surface normal vector field $\boldsymbol{\pi}_{\mathrm{n}}(p)$ are interpolated independently using B-splines, the orthogonality between $\boldsymbol{\pi}_{\mathrm{n}}(p)$ and the path tangent $\boldsymbol{\pi}'(p)$ is lost. To recover this property, a surface-based orthonormalized frame $(\tilde{\mathbf{e}}_1, \tilde{\mathbf{e}}_2, \tilde{\mathbf{e}}_3)(p)$ is introduced

$$\tilde{\mathbf{e}}_1(p) = \boldsymbol{\pi}'(p) \tag{37a}$$

$$\tilde{\mathbf{e}}_3(p) = \frac{\boldsymbol{\pi}_{\mathrm{n}}(p) - \boldsymbol{\pi}_{\mathrm{n}}^{\mathrm{T}}(p)\tilde{\mathbf{e}}_1(p)\tilde{\mathbf{e}}_1(p)}{\|\boldsymbol{\pi}_{\mathrm{n}}(p) - \boldsymbol{\pi}_{\mathrm{n}}^{\mathrm{T}}(p)\tilde{\mathbf{e}}_1(p)\tilde{\mathbf{e}}_1(p)\|_2} \tag{37b}$$

$$\tilde{\mathbf{e}}_2(p) = \tilde{\mathbf{e}}_3(p) \times \tilde{\mathbf{e}}_1(p) , \tag{37c}$$

which adjusts and normalizes the normal vector field $\boldsymbol{\pi}_{\mathrm{n}}(p)$ accordingly. Note that the assumption of arc-length parametrized paths $\boldsymbol{\pi}(p)$ was used in (37a) and the orthonormalized frame (37) is of class $\mathcal{C}^2$ due to the $\mathcal{C}^3$-smoothness of $\boldsymbol{\pi}(p)$.

2) Discrete-Time Parallel Contact Frame: The frame $\mathcal{C}(p)$ from Section III-E3 describes the contact frame for the draping roll. This specific frame was introduced to prevent any rotations

of the draping roll around the surface normal vector. The unit vector field $\mathbf{e}_1(p)$ is a parallel vector field w.r.t. the surface σ. According to (5), the derivative of this parallel vector field $\mathbf{e}_1(p)$ only exhibits a component normal to the surface. Similarly, the parallel transport frame of a path prevents rotations around the path tangent vector and the derivatives of the two path normal vectors are scalar multiples of the path tangent vector [17]. Hence, the discrete-time implementation for the parallel transport frame according to [17] can be adapted to the parallel contact frame introduced in this work. The discrete-time tangent vector field $\mathbf{e}_{1,k}$, with a suitable initial tangent vector $\mathbf{e}_{1,0} = \tilde{\mathbf{e}}_1(p_0)$, is calculated from the normal vector field $\mathbf{e}_{3,k}$ using [17], [35]

$$\mathbf{e}_{3,k} = \tilde{\mathbf{e}}_3(p_k) \tag{38a}$$

$$\mathbf{e}_{1,k} = \frac{\mathbf{e}_{1,k-1} - \mathbf{e}_{3,k}^{\mathrm{T}}\mathbf{e}_{1,k-1}\mathbf{e}_{3,k}}{\sqrt{1 - \left(\mathbf{e}_{3,k}^{\mathrm{T}}\mathbf{e}_{1,k-1}\right)^2}} \tag{38b}$$

$$\mathbf{e}_{2,k} = \mathbf{e}_{3,k} \times \mathbf{e}_{1,k} . \tag{38c}$$

Note that, compared to the parallel transport frame in [17] and [35], the roles of the tangent and normal vector in (38b) are interchanged. It is further worth noting that the integration of (15) is not required, as the discrete-time parallel contact frame can be computed online using (38).

3) Discrete-Time Projection Operator: The constraint of the projection operator $\mathrm{P}(\mathbf{y}_{\mathrm{p}})$ in (22) is solved numerically with the NEWTON iteration

$$p_{k,i} = p_{k,i-1} - \frac{f(p_{k,i-1})}{f'(p_{k,i-1})} \tag{39}$$

with $i = 1, 2, \ldots,$ and $f(p_{k,i}) = (\mathbf{y}_{\mathrm{p}} - \boldsymbol{\pi}(p_{k,i}))^{\mathrm{T}}\mathbf{e}_{1,k}$. The iteration is initialized with the path parameter of the previous time step, i.e. $p_{k,0} = p_{k-1}^*$ and terminates with $|p_{k,i} - p_{k,i-1}| < \varepsilon$, $\varepsilon > 0$. The resulting path parameter, denoted by p_k^*, indicates the projected position on the path. Note that due to Remark 5, a surface-based path π can only exhibit one solution of (22). Thus, for this case, the minimum distance criterion $\|\mathbf{y}_{\mathrm{p}} - \boldsymbol{\pi}(p^*)\|_2$ is not considered. Finally, the integral in (26) is solved numerically using the explicit EULER method

$$\xi_{1,k} = \xi_{1,k-1} + (p_k^* - p_{k-1}^*)(\boldsymbol{\pi}'(p_k^*))^{\mathrm{T}}\mathbf{e}_{1,k} . \tag{40}$$

VI. EXPERIMENTAL RESULTS

The surface-based path following control concept from Section IV is demonstrated on a 3-D-printed object, as shown in Fig. 7: The paths of the pre-cut tapes in Fig. 7(a) are mapped onto the discrete surface of the 3-D object in Fig. 7(b). The tape application result is depicted in Fig. 7(c). A video of the complete demonstration can be found at `www.acin.tuwien.ac.at/52f5`.

In this work, the tape application paths computed using Algorithm 1 are sampled with a grid of $\Delta p = 4$ mm. Nevertheless, the absolute errors of the interpolated B-splines are below 0.1 mm for positions and below 50 mrad for the orientation of the surface-based orthonormalized frame, which is computed from (37). These small deviations are admissible for the considered

10129

This article has been accepted for inclusion in a future issue of this journal. Content is final as presented, with the exception of pagination.

10   IEEE TRANSACTIONS ON ROBOTICS
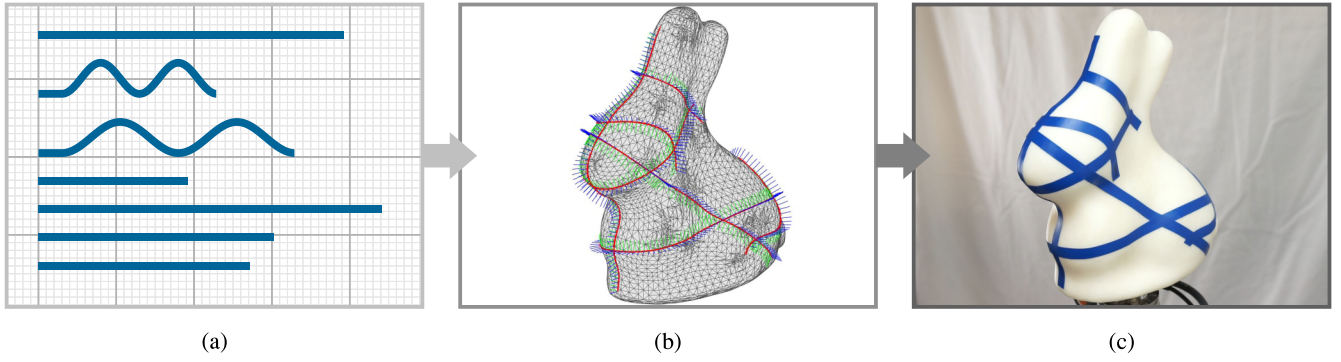

Fig. 7.   Experimental results of the tape application process on a 3-D-printed object. (a) Pre-cut tapes. (b) Projected paths on 3-D object. (c) Completed tape application.
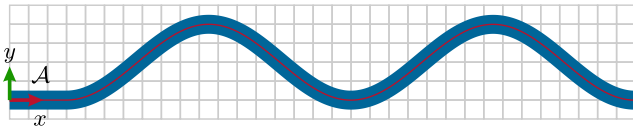

Fig. 8.   Tape (blue) and curved tape application path (red) for the experimental results shown in Fig. 9.

TABLE I
CONTROLLER PARAMETERS

Symbol	Value	Unit
$k_1^{\mathrm{d}}, k_2^{\mathrm{d}}, k_4^{\mathrm{d}}, k_6^{\mathrm{d}}$	900	N/m
$d_1^{\mathrm{d}}, d_2^{\mathrm{d}}, d_4^{\mathrm{d}}, d_6^{\mathrm{d}}$	60	N s/m
$m_1^{\mathrm{d}}, \dots, m_6^{\mathrm{d}}$	1	kg
k_3^{d}	400	N/m
d_3^{d}	40	N s/m
k_5^{d}	0	N/m
d_5^{d}	4	N s/m
$\mathbf{K}_{\mathrm{n}}$	$\mathrm{diag}(1,1,1,1,1,1,1)$	N/m
$\mathbf{D}_{\mathrm{n}}$	$\mathrm{diag}(2,2,2,2,2,2,2)$	N s/m

process and are compensated by the compliant draping roll. Note that smaller sampling grids Δp lead to smaller absolute errors, but also to paths with higher curvatures.

In the following, the application of a single pre-cut tape with a curved path, depicted in Fig. 8, is described in more detail. The measured force and torque signals of the F/T sensor are used to verify the interaction forces only and are not used for feedback in these experiments. To obtain a quasi-static estimate for $\hat{\mathbf{f}}_{\mathrm{e}}$, the gravitational force of the 3-D object is subtracted from the tool-side F/T measurement and the net force is transformed into the current contact frame $\mathcal{C}(p^*)$ [25]. The relevant signals of the tape application process are shown in Fig. 9, whereas all controller parameters are listed in Table I. The graphs in Fig. 9 are subdivided into three phases ①–③.

1) *Contact establishment:* Due to the control concept and the chosen contact frame, the coordinate ξ_3 corresponds to the movement normal to the surface. Using a $\mathcal{C}^2$-trajectory from $\xi_3 = 30\,\mathrm{mm}$ to $\xi_3 = 14\,\mathrm{mm}$, the 3-D object approaches the draping roll and comes into contact. The

surface normal contact force $\hat{f}_{\mathrm{e},3}$ is approximately 3N, while the other forces and torques remain close to zero.

2) *Impedance-based tape application:* In the second phase, the tape application is performed using the surface-based path following controller (33), (35), and (36). In path coordinates $\hat{\mathbf{y}}$, the contact point moves from $\xi_1 = 0\,\mathrm{mm}$ to $\xi_1 = 322\,\mathrm{mm}$ with a velocity of $\dot{\xi}_1 = 30\,\mathrm{mm/s}$ using a $\mathcal{C}^2$-trajectory. The lateral motion along the draping roll axis is given by $\xi_2^{\mathrm{d}} = -\pi_1(p)$, which correctly takes into account the lateral movement of the contact point, as illustrated in Fig. 8, cf. Fig. 3. While the control errors $\hat{e}_1$ and $\hat{e}_2$ of the geodesic direction ξ_1 and the lateral direction ξ_2 stay below 1.2 mm, the controller adjusts the position ξ_3 along the surface normal according to the impedance model. Thus, the control strategy is able to comply with uncertainties related to the 3-D object and with the position errors of the robot manipulator. Throughout the process, the surface normal force $\hat{f}_{\mathrm{e},3}$ remains the dominant component. While the surface tangent forces $\hat{f}_{\mathrm{e},1}$ and $\hat{f}_{\mathrm{e},2}$ are mostly below 1 N, the estimated torques $\hat{f}_{\mathrm{e},4}, \hat{f}_{\mathrm{e},5}$, and $\hat{f}_{\mathrm{e},6}$ stay well below 150 mN m.

3) *Contact release:* Finally, the contact between draping roll and 3-D object is released by moving the 3-D object from $\xi_3 = 14\,\mathrm{mm}$ to $\xi_3 = 30\,\mathrm{mm}$ again. Note that after release, minor estimated torques $\hat{f}_{\mathrm{e},4}, \hat{f}_{\mathrm{e},5}$, and $\hat{f}_{\mathrm{e},6}$ remain due to imperfect compensation of the payload mass.

VII.   CONCLUSION

In this article, a surface-based path following control concept was introduced for the application of (curved) pre-cut adhesive tapes on freeform 3-D objects. For this, a novel parallel contact frame with a parallel projection operator was developed to prevent rotations of the draping roll around the surface normal axis, which is required for a wrinkle-free tape application result. The (curved) surface-based tape application paths were calculated as solutions to an initial value problem in the surface coordinates with a given starting point, tangent direction, and local geodesic curvature along the path. In this way, the 2-D tape application paths were mapped onto the freeform 3-D object. Moreover, details on the discrete-time implementation using discrete-space

This article has been accepted for inclusion in a future issue of this journal. Content is final as presented, with the exception of pagination.

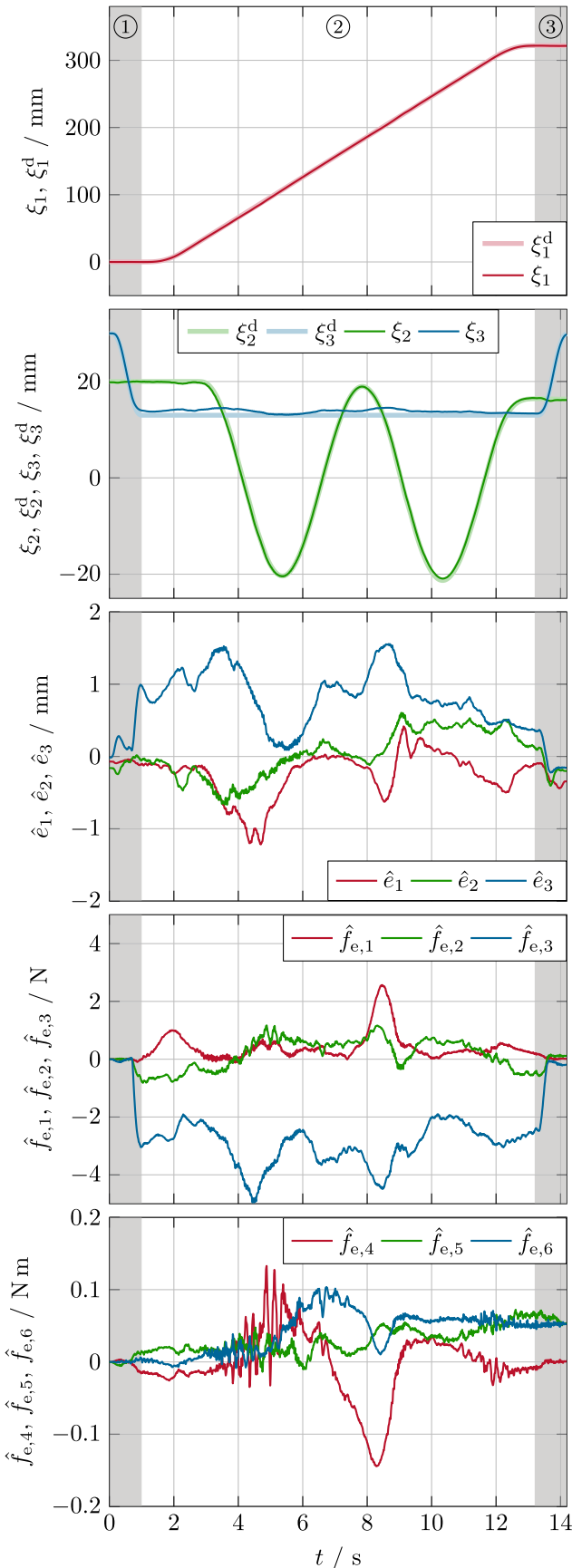HARTL-NESIC *et al.*: SURFACE-BASED PATH FOLLOWING CONTROL

11

Fig. 9. Experimental results of the tape application process. ① Contact establishment. ② Impedance-based tape application. ③ Contact release.

surfaces were given. Measurement results on an experimental setup showed a good performance and demonstrated the practical relevance of the proposed approach.

Future work aims at improving the passive tape application tool to automatically feed the pre-cut tapes to the required starting position for the first contact with the 3-D object. Additionally, using collision-free trajectory planning, the robot can move the 3-D object to the corresponding starting position without user intervention. Finally, automatic handling of the single-axis redundancy, which is present due to the cylindrical shape of the draping roll, can be incorporated into the control concept in the future. This type of redundancy occurs in many other industrial processes like, e.g. laser cutting, painting, and polishing.

REFERENCES

[1] H. B. Olsen and J. J. Craig, "Automated composite tape lay-up using robotic devices," in *Proc. IEEE Int. Conf. Robot. Autom.*, Atlanta, GA, USA, 1993, pp. 291–297.

[2] R. Buckingham and G. Newell, "Automating the manufacture of composite broadgoods," *Composites Part A, Appl. Sci. Manuf.*, vol. 27A, no. 3, pp. 191–200, 1996.

[3] A. Björnsson, M. Jonsson, and K. Johansen, "Automated material handling in composite manufacturing using pick-and-place systems—A review," *Robot. Comput.–Integr. Manuf.*, vol. 51, pp. 222–229, 2018.

[4] G. Fantoni *et al.*, "Grasping devices and methods in automated production processes," *CIRP Ann., Manuf. Technol.*, vol. 63, no. 2, pp. 679–701, 2014.

[5] C. Löchte *et al.*, "Form-flexible handling technology for automated pre-forming," in *Proc. Int. Conf. Composite Materials*, Montreal, Canada, 2013, pp. 2130–2141.

[6] G. Reinhart and G. Straßer, "Flexible gripping technology for the auto-mated handling of limp technical textiles in composites industry," *Prod. Eng.*, vol. 5, no. 3, pp. 301–306, 2011.

[7] S. Flixeder, T. Glück, and A. Kugi, "Force-based cooperative handling and lay-up of deformable materials: Mechatronic design, modeling, and control of a demonstrator," *Mechatronics*, vol. 47, pp. 246–261, 2017.

[8] Samba Pro. Cevotec GmbH. [Online]. Available: https://www.cevotec.com/. Accessed on: Jun. 11, 2020.

[9] W. Van Loock, G. Pipeleers, M. Diehl, J. De Schutter, and J. Swevers, "Optimal path following for differentially flat robotic systems through a geometric problem formulation," *IEEE Trans. Robot.*, vol. 30, no. 4, pp. 980–985, Aug. 2014.

[10] G.-C. Chiu and M. Tomizuka, "Contouring control of machine tool feed drive systems: A task coordinate frame approach," *IEEE Trans. Control Syst. Technol.*, vol. 9, no. 1, pp. 130–139, Jan. 2001.

[11] T. Faulwasser, T. Weber, P. Zometa, and R. Findeisen, "Implementation of nonlinear model predictive path-following control for an industrial robot," *IEEE Trans. Control Syst. Technol.*, vol. 25, no. 4, pp. 1505–1511, Jul. 2017.

[12] C. Nielsen, C. Fulford, and M. Maggiore, "Path following using transverse feedback linearization: Application to a Maglev positioning system," in *Proc. Amer. Control Conf.*, St. Louis, MO, USA, 2009, pp. 3045–3050.

[13] A. Hladio, C. Nielsen, and D. Wang, "Path following for a class of mechanical systems," *IEEE Trans. Control Syst. Technol.*, vol. 21, no. 6, pp. 2380–2390, Nov. 2013.

[14] V. A. Toponogov, *Differential Geometry of Curves and Surfaces*. Boston, MA, USA: Birkhäuser, 2006.

[15] R. J. Gill, D. Kulić, and C. Nielsen, "Spline path following for redundant mechanical systems," *IEEE Trans. Robot.*, vol. 31, no. 6, pp. 1378–1392, Dec. 2015.

[16] R. L. Bishop, "There is more than one way to frame a curve," *Amer. Math. Monthly*, vol. 82, no. 3, pp. 246–251, 1975.

[17] B. Bischof, T. Glück, and A. Kugi, "Combined path following and com-pliance control for fully actuated rigid body systems in 3-D space," *IEEE Trans. Control Syst. Technol.*, vol. 25, no. 5, pp. 1750–1760, Sep. 2017.

[18] I. Kaminer, A. Pascoal, E. Xargay, N. Hovakimyan, C. Cao, and V. Dobrokhodov, "Path following for unmanned aerial vehicles using $\mathcal{L}_1$ adaptive augmentation of commercial autopilots," *J. Guid., Control, Dyn.*, vol. 33, no. 2, pp. 550–564, 2010.

[19] T. Oliveira, P. Encarnação, and A. P. Aguiar, "Moving path following for autonomous robotic vehicles," in *Proc. Eur. Control Conf.*, Zurich, Switzerland, 2013, pp. 3320–3325.

[20] B. Bischof, T. Glück, M. Böck, and A. Kugi, "A path/surface following control approach to generate virtual fixtures," *IEEE Trans. Robot.*, vol. 34, no. 6, pp. 1577–1592, Dec. 2018.

[21] M. Elkington, C. Ward, and K. D. Potter, "Automated layup of sheet prepregs on complex moulds," in *Proc. Int. Soc. Advance. Mater. Process Eng. Tech. Conf.*, Long Beach, CA, USA, Jun. 2016, pp. 1–16.

[22] D. Do, L. Ma, R. Paton, S. John, and I. Herszberg, "Automated consolidation during the manufacture of composite material based components," in *Proc. Int. Conf. Composite Materials*, Paris, France, 1999, pp. 1–7.

[23] N. Hayashi, T. Tomizawa, T. Suehiro, and S. Kudoh, "Dual arm robot fabric wrapping operation using target lines," in *Proc. IEEE Int. Conf. Robot. Biomimetics*, Bali, Indonesia, 2014, pp. 2185–2190.

[24] C. Ott, *Cartesian Impedance Control of Redundant and Flexible-Joint Robots*. Berlin, Germany: Springer, 2008.

[25] B. Siciliano, L. Sciavicco, L. Villani, and G. Oriolo, *Robotics: Modelling, Planning and Control*. London, U.K.: Springer, 2010.

[26] M. P. Do Carmo, *Differential Geometry of Curves and Surfaces*. Englewood Cliffs, NJ, USA: Prentice-Hall, 1976.

[27] J. Scholliers and H. Van Brussel, "Computer-integrated filament winding: Computer-integrated design, robotic filament winding and robotic quality control," *Composites Manuf.*, vol. 5, no. 1, pp. 15–23, 1994.

[28] L. Perko, *Differential Equations and Dynamical Systems*, vol. 7, 3rd ed. J. Marsden, L. Sirovich, and M. Golubitsky, (Series in Applied Mathematics), Eds. New York, NY, USA: Springer, 2001.

[29] L. Yan, Z. C. Chen, Y. Shi, and R. Mo, "An accurate approach to roller path generation for robotic fibre placement of free-form surface composites," *Robot. Comput.-Integr. Manuf.*, vol. 30, no. 3, pp. 277–286, 2014.

[30] A. Dietrich, C. Ott, and A. Albu-Schäffer, "An overview of null space projections for redundant, torque controlled robots," *Int. J. Robot. Res.*, vol. 34, no. 11, pp. 1385–1400, 2015.

[31] G. R. Kumar, P. Srinivasan, V. D. Holla, K. Shastry, and B. Prakash, "Geodesic curve computations on surfaces," *Comput.-Aided Geometric Des.*, vol. 20, no. 2, pp. 119–133, 2003.

[32] J. C. Butcher, *Numerical Methods for Ordinary Differential Equations*, 3rd ed. Chichester, U.K.: Wiley, 2016.

[33] L. Piegl and W. Tiller, *The NURBS Book*, 2nd ed. Berlin, Germany: Springer, 1997.

[34] M.-J. Kim, M.-S. Kim, and S. Y. Shin, "A general construction scheme for unit quaternion curves with simple high order derivatives," in *Proc. Special Int. Group Graph. Interactive Techn.*, Los Angeles, CA, USA, 1995, pp. 369–376.

[35] A. J. Hanson, *Visualizing Quaternions* (Interactive 3D Technology), D. Eberly, Ed. San Francisco, CA, USA: Morgan Kaufmann, 2006.

Christian Hartl-Nesic (Member, IEEE) received the Dipl.-Ing. degree and Ph.D. (Dr.techn.) degree in electrical engineering from the TU Wien, Vienna, Austria, in 2016 and 2020, respectively.

He is currently working as Postdoctoral Researcher with the Automation and Control Institute, TU Wien. His main research interests include novel control, teach-in, and usage concepts for robotics in a wide range of industrial applications as well as human–robot interaction.

Tobias Glück (Member, IEEE) received the Diploma degree in engineering cybernetics from the University of Stuttgart, Stuttgart, Germany, in 2007, and the Ph.D. (Dr.techn.) degree in electrical engineering from the TU Wien, Vienna, Austria, in 2013.

He is with the AIT Austrian Institute of Technology GmbH, Vienna, and is the Head with the Complex Dynamic Systems Research Group, Center for Vision and Automation and Control. He has many years of experience in application-oriented research. His work focuses on "thinking in systems" and the automation of mechatronic components, manufacturing processes, and products.

Andreas Kugi (Senior Member, IEEE) received the Dipl.-Ing. degree in electrical engineering from the Graz University of Technology, Graz, Austria, in 1992, and the Ph.D. degree in control engineering and the Habilitation degree in automatic control and control theory from Johannes Kepler University (JKU), Linz, Austria, in 1995 and 2000, respectively.

He was an Associate Professor with JKU from 2000 to 2002 and a Full Professor with Saarland University, Saarbrücken, Germany, from 2002 to 2007. Since 2007, he has been the Head with the Automation and Control Institute, TU Wien, Vienna, Austria, and since 2017, he has also been the Head with the Center for Vision, Automation and Control, AIT Austrian Institute of Technology GmbH, Vienna. His main research interests include the modeling, control, and optimization of complex dynamical systems, the mechatronic system design, as well as robotics and process automation.

Prof. Kugi is a Full Member of the Austrian Academy of Sciences and a Member of the German National Academy of Science and Engineering (acatech).